Modern Management Science & Engineering
ISSN ISSN 2052-2576
Vol. 8, No. 3, 2026
www.scholink.org/ojs/index.php/mmse

Original Paper

Influence of Involute and Cycloid-Pin Profile Modification on the Dynamic Transmission Characteristics of the RV Reducer

Wenwen Du & Yinghui Zhang*

Dalian Jiaotong University, Dalian,Liaoning, China

* Corresponding Author

Received: April 29, 2026 Accepted: May 22, 2026 Online Published: June 23, 2026

doi:10.22158/mmse.v8n3p21 URL: http://dx.doi.org/10.22158/mmse.v8n3p21

Abstract

To clarify the combined influence of involute and cycloidal profile modifications on RV reducer dynamics, a coupled multibody model including the involute gear pair, cycloid-pin pair, and bearing-support system was developed. Composite meshing error, time-varying meshing stiffness, and external load were considered, while meshing stiffness and contact parameters from Romax were introduced to improve engineering fidelity; the dynamic response was solved using the Gill integration method. Comparative analyses were conducted for involute profile modification, cycloidal moved-distance equidistant modification, and cycloidal pressure-angle modification in terms of meshing stiffness, load distribution, contact stress, transmission error, and vibroacoustic behavior. Involute modification reduced the maximum meshing stiffness from 1.33×10^5 *to N/mm (17.3%) and suppressed stiffness fluctuation during the single-to-double tooth transition. For the cycloid-pin stage, pressure-angle modification lowered peak contact stress from about 1600 to 1100 MPa (31.3%). Although transmission error changed only slightly, the involute plus pressure-angle scheme achieved the best overall vibroacoustic performance, reducing the dominant low-frequency acoustic peak by about 11 dB(A) and equivalent acoustic radiation power by about 60%, providing guidance for RV reducer profile design and dynamic optimization.*

Keywords

RV reducer, precision transmission, tooth profile modification, cycloidal-pin wheel, dynamic performance

1. Introduction

RV (Rotate Vector) reducers are core transmission components in robotic joint drive systems, and their vibration and noise performance directly affects motion accuracy and system stability [1-4]. Owing to

their high transmission ratios, high stiffness, strong load-bearing capacity, compact structure, and small backlash, RV reducers have been widely used in industrial robots and high-performance joint actuation systems [1,2,5]. With the increasing deployment of humanoid robots featuring high-power and wide-range joints, the requirements for compact, high-stiffness, and smooth joint transmissions have become more stringent, which further elevates the performance demands placed on precision reducers [24]. As robotic systems continue to develop toward higher precision and higher dynamic performance, vibration and noise generated during reducer operation have become increasingly important factors limiting transmission smoothness, positioning accuracy, and long-term reliability [2-4,6]. Compared with conventional single-stage transmissions, an RV reducer integrates both involute gear pairs and cycloid-pin pairs together with multiple bearing-support elements. The significant differences in their geometry and meshing kinematics lead to complex multi-body coupled vibration characteristics. Meshing error, time-varying meshing stiffness, tooth-side clearance, manufacturing and assembly deviations, and support flexibility interact with one another, thereby affecting dynamic load transfer, transmission error, and noise radiation [3,4,6-8].

In recent years, substantial research has been devoted to dynamic modeling, transmission performance evaluation, and tooth profile modification of RV reducers [3-8,10-13]. Review studies have systematically summarized the design, analysis, and performance evaluation of precision reducers for industrial robots, emphasizing transmission accuracy, torsional stiffness, vibration, and noise as key concerns in practical applications [1,2]. In dynamic modeling, lumped-parameter and translational-torsional coupled models that consider meshing error, time-varying meshing stiffness, tooth-side clearance, and support stiffness have been developed to reveal the vibration response and stability characteristics of the system [3,4,6,8]. With respect to transmission performance, rotational transmission error, tooth-side clearance, and torsional stiffness have been widely adopted as key indices for precision evaluation and structural optimization [5,7,10,12]. Meanwhile, tooth profile modification has been widely recognized as an effective approach to improve meshing conditions, optimize load distribution, and suppress vibration and noise. Recent studies have investigated the effects of profile modification and load on transmission characteristics [5], ADAMS-based transmission analysis of RV reducers [10], piecewise modification of cycloidal gears [11], and two-stage tooth profile modification for vibration reduction [13]. These studies have provided valuable insights into the local contact behavior and transmission characteristics of RV reducers under different operating conditions.

However, several issues remain insufficiently addressed. Most existing studies focus on a single meshing stage, local contact performance, or individual modification parameters, while relatively limited attention has been paid to the coupled interaction among the involute gear stage, cycloid-pin stage, and bearing-support system within an integrated RV reducer [4,6,8,10,11]. For an RV reducer, the involute gear stage, cycloid-pin stage, and bearing-support structure are interconnected through coupled stiffness, error excitation, and load transfer. Therefore, the influence of different tooth profile modification combinations should be evaluated at the whole-machine level rather than only at the local

contact level. In particular, the combined dynamic effects of involute profile modification and different cycloidal modification strategies on meshing excitation, load distribution, transmission error, and vibration-noise-related response have not yet been sufficiently clarified within a unified analytical framework [9-11,13].

To address these issues, this study develops a coupled multibody dynamic model of an RV reducer for humanoid robot joints [25] by integrating the involute gear pair, cycloid-pin pair, and bearing-support system. The model incorporates comprehensive meshing errors, time-varying meshing stiffness, external load excitation, and contact parameters extracted from Romax under different modification schemes. Based on this framework, involute profile modification, cycloidal equidistant modification, and cycloidal pressure-angle modification are comparatively evaluated in terms of meshing stiffness, load distribution, contact stress, transmission error, equivalent acoustic radiation power, and a vibration power flow index. The main contributions are threefold: (1) establishing a unified dynamic framework for the RV reducer; (2) systematically comparing involute and cycloidal modification combinations within the same model; and (3) clarifying how profile modification affects dynamic excitation, load transfer, and vibration-noise response, thereby providing a theoretical basis for the low-vibration and low-noise design of RV reducers.

2. Models and Methods

2.1 Structure of the RV Reducer and Research Object

Figure 1 presents a simplified dynamic model of a straight-tooth external meshing unit [14]. Projecting the gear vibration displacement along the meshing line direction, the relative total deformation of the gear pair along this projection line is

$$\delta_o=\mathbf{V}_o\mathbf{x}_o-e_o \tag{1}$$

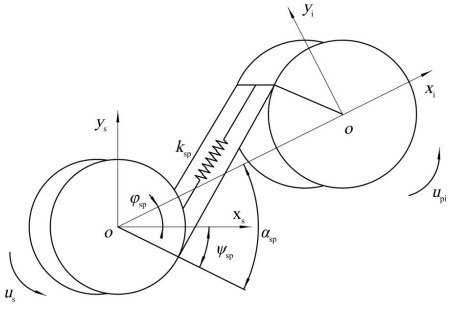

Figure 1. Simplified Dynamic Model of Straight-tooth External Meshing Unit

In the formula, $x_o=\{x_s,y_s,\theta_s,x_p,y_p,\theta_p\}$ denotes the displacement vector of the sun gear and planet gear unit node; represents the comprehensive meshing error in the normal direction of the external gear pair; is the projection vector of the displacement in each direction of the external gear pair converted to the meshing line direction:

$$V_o=[sin\psi_{sp},cos\psi_{sp},r_{bs},-sin\alpha_{sp},-cos\alpha_{sp},r_{bp}] \tag{2}$$

In the formula, and denote the base circle radii of the sun gear and planet gear respectively; is the angle between the meshing line of the planet gear and sun gear and the axis.

$$\psi_{sp}=\alpha_{spi}-\varphi_{pi} \tag{3}$$

In the formula, denotes the meshing angle of the i-th planetary gear, and denotes the installation phase angle of the i-th planetary gear.

According to Newton's second law, the differential equation of motion of the external meshing unit can be obtained:

$$\begin{cases} m_s\ddot{x}_s+(c_{sp}\dot{\delta}_o+k_{sp}\delta_o)sin\psi_{sp}=0 \\ m_s\ddot{y}_s+(c_{sp}\dot{\delta}_o+k_{sp}\delta_o)cos\psi_{sp}=0 \\ I_s\ddot{\theta}_s-(c_{sp}\dot{\delta}_o+k_{sp}\delta_o)r_{bs}=T_s \\ m_p\ddot{x}_p-(c_{sp}\dot{\delta}_o+k_{sp}\delta_o)sin\alpha_{sp}=0 \\ m_p\ddot{y}_p+(c_{sp}\dot{\delta}_o+k_{sp}\delta_o)cos\alpha_{sp}=0 \\ I_p\ddot{\theta}_p+(c_{sp}\dot{\delta}_o+k_{sp}\delta_o)r_{bp}=-T_p \end{cases} \tag{4}$$

where are the masses of the sun gear and planet gear respectively, are the moments of inertia of the sun gear and planet gear respectively, is the combined meshing stiffness of the external gear pair, and is the meshing damping of the external gear pair.

Substituting equations (1) to (3) into equation (4), we obtain the differential equations of motion for the external meshing unit:

$$M_o\ddot{x}_o+C_o(\dot{x}_o-\dot{e}_o)+K_o(x_o-e_o)=F_o \tag{5}$$

In the formula, is the mass matrix of the external meshing unit; C_o is the damping matrix of the external meshing unit; K_o is the stiffness matrix of the external meshing unit; e_o and are the column vectors of equivalent displacement and equivalent velocity respectively after decomposing the comprehensive meshing error of the external meshing unit in each direction.

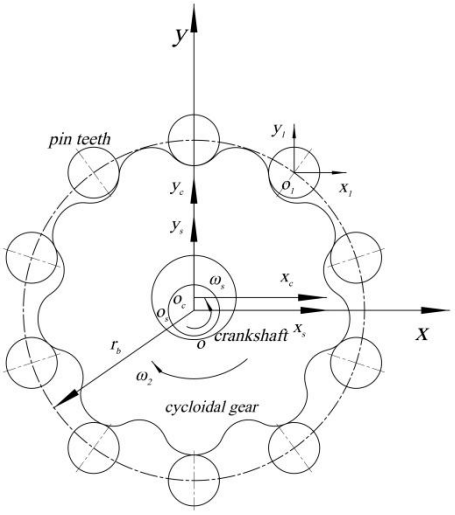

Figure 2. Cycloid Pinwheel Engagement Model

As illustrated in Figure 2, a multi-body dynamic model of a cycloid-pin transmission system is constructed in a generalized coordinate system [15]. In this model, the input shaft is fixed and rotates, with its angular velocity denoted by ω_s, and its local coordinate system is located at the rotation center. The crankshaft has an eccentricity of e, positioned horizontally. The cycloidal gear's local coordinate system is centered at its geometric center, with its rotational angular velocity represented by ω_2. The cycloidal gear's rotation center on the crankshaft serves as the origin of its local coordinate system. Additionally, the local coordinate system of the i-th pin gear pin is located at the pinion gear pin's geometric center. In this model, there are individuals of rigid bodies: the crankshaft, the cycloidal gear, and individual of the pinion gear. Therefore, the generalized coordinate vector of the system can be expressed as

$$q=(x_s,y_s,\theta_s,x_c,y_c,\theta_c,x_1,y_1,\theta_1,\ldots,x_i,y_i,\theta_i,\ldots,x_N,y_N,\theta_N)^T \quad i=1,2,\ldots,N \tag{6}$$

In the formula, represent the position coordinates of the crankshaft's local coordinate system origin in the generalized coordinate system; x_c,y_c denote the position coordinates of the cycloidal gear's local coordinate system origin in the generalized coordinate system; x_i,y_i indicate the position coordinates of each pin's local coordinate system origin in the generalized coordinate system; $\theta_s,\theta_c,\theta_i$ are the relative rotation angles of the crankshaft, cycloidal gear, and each pin's local coordinate system to the generalized coordinate system.

The system constraint equations can be expressed as

$$\boldsymbol{\Phi}=\begin{bmatrix} x_s \\ y_s \\ x_s+e\cos\theta_s-x_c \\ y_s+e\sin\theta_s-y_c \\ x_i-r_b\cos\theta_i \\ y_i-r_b\sin\theta_i \\ \theta_s-\theta_0-\omega_s t \\ \theta_i \end{bmatrix}=0 \tag{7}$$

where is the radius of the pinion tooth distribution circle; θ_0 is the initial rotation angle position of the crankshaft; t is the time.

In the framework of multi-body dynamics, the mass inertia matrix, the Jacobian matrix of constraint equations and the generalized force vector of the system are sorted out and substituted into the multi-body dynamics equations.

$$\begin{bmatrix} \boldsymbol{m} & \boldsymbol{\Phi}_q^T \\ \boldsymbol{\Phi}_q & 0 \end{bmatrix}\begin{bmatrix} \ddot{\boldsymbol{q}} \\ \boldsymbol{\lambda} \end{bmatrix}=\begin{bmatrix} \boldsymbol{Q} \\ \boldsymbol{\Phi}_q\ddot{\boldsymbol{q}} \end{bmatrix} \tag{8}$$

where is the mass inertia matrix of the system, is the Jacobian matrix of the constraint equations, is the generalized acceleration vector, is the Lagrange multiplier, and is the generalized force vector of the system.

The planetary frame not only functions as the output component of the system but also serves as the support for the planetary gears. Let the deformation of the planetary frame be defined as δ_c, expressed as $\delta_c=V_c x_c$, where denotes the displacement vector of each node of the planetary frame unit, and represents the projection vector of the displacement in each direction under the overall coordinate system of the planetary frame. It can be expressed as

$$\begin{cases} V_c^x=[cos\phi_{pi},sin\phi_{pi},0,-1,0,0] \\ V_c^y=[-sin\phi_{pi},cos\phi_{pi},r_c,0,-1,0] \end{cases} \tag{9}$$

Therefore, the differential equation of motion for the planetary frame unit is

$$\begin{cases} m_c\ddot{x}_c+k_{px}\delta_c^x cos\phi_{pi}-k_{py}\delta_c^y sin\phi_{pi}=0 \\ m_c\ddot{y}_c+k_{px}\delta_c^x cos\phi_{pi}+k_{py}\delta_c^y sin\phi_{pi}=0 \\ I_c\ddot{\theta}_c-k_{py}\delta_c^y=-T_c \\ m_p\ddot{x}_p-k_{px}\delta_c^x=0 \\ m_p\ddot{y}_p-k_{py}\delta_c^y=0 \\ I_p\ddot{\theta}_p=0 \end{cases} \tag{10}$$

where are the masses of the planetary carrier and the planetary gear respectively; are the moments of inertia of the planetary carrier and the planetary gear about their respective rotation centers; are the support stiffness of the planetary carrier to the planetary gear in the direction of and the direction of respectively; φ_{pi} are the mounting phase angles of the planetary gear.

The equations (10) can be organized into a matrix form as follows:

$$\boldsymbol{M}_c\ddot{\boldsymbol{x}}_c+\boldsymbol{K}_c\boldsymbol{x}_c=\boldsymbol{F}_c \tag{11}$$

where M_c is the mass matrix of the planetary gear unit, is the stiffness matrix of the planetary gear unit, and is the column vector of the external forces acting on the planetary gear unit.

The rolling bearing is usually used in the RV reducer. Because the bearing is small in mass, it is not included in the mass of the bearing, but the bearing provides support stiffness to each component, which cannot be ignored. Considering the relative motion between the inner and outer rings of the bearing, a local coordinate system is constructed with the bearing center as the origin, and the radial, tangential, and axial axes as the coordinate axes.

The bearing support unit primarily withstands the following forces: the meshing force generated by the cycloidal gear and pinion is transmitted to the rotating arm bearing; the support bearings distributed on both sides of the crankshaft balance the rotating arm bearing and the load; the main bearing bears the forces from the two-side planetary carrier and pinion housing. Given the complex load distribution across the bearings in the RV reducer, the detailed force analysis process is detailed in reference [16], which will not be elaborated here.

According to Newton's second law, the dynamic equation of the bearing support unit can be expressed as:

$$\boldsymbol{M}\ddot{\boldsymbol{x}}+\boldsymbol{C}\dot{\boldsymbol{x}}+\boldsymbol{K}\boldsymbol{x}=\boldsymbol{F} \tag{12}$$

The matrix components are: is the equivalent mass matrix of the bearing support unit, which accounts for the mass distribution of the inner and outer rings and connecting components; is the damping matrix, reflecting the frictional and material damping characteristics of the bearing; is the stiffness matrix, comprising is radial, is tangential, and is axial stiffness; is the relative displacement vector of the inner and outer rings, corresponding to radial, tangential, and axial displacements respectively; and is the external force vector.

2.2 Coupled Dynamics Model

The dynamic model of the subsystem is constructed by the meshing unit, the support unit and the cycloid-pin transmission unit. The model is assembled by the relationship of the degree of freedom of the nodes. The influence of the profile modification on the dynamic of the whole system is considered. The excitation of

meshing error, the excitation of time-varying meshing stiffness and the external load are included in the dynamic equation of the whole system.

$$\boldsymbol{M\ddot{q}+C\dot{q}+Kq=F(t)} \tag{13}$$

The formula includes: is the system mass matrix, is the system damping matrix, is the system stiffness matrix, is the system generalized displacement vector, is the generalized velocity vector,$\ddot{q}$ is the generalized acceleration vector, $F(t)$ is the external excitation vector, which includes meshing error excitation, time-varying meshing stiffness excitation, and external loads.

To study the vibration characteristics of the system, the generalized displacement of the system is decomposed into the sum of the reference motion and the small vibration displacement. Therefore,

$$q(t)=q_0(t)+x(t) \tag{14}$$

where: is the reference motion (or equilibrium position) of the system in the average transmission state; $x(t)$ is the small vibration displacement vector of the system relative to the reference motion.

Substituting Equation (14) into the system's overall dynamic equation (13), and performing perturbation analysis near the equilibrium position or periodic steady-state reference orbit while neglecting higher-order small quantities, we obtain the system's vibration dynamic equation:

$$\boldsymbol{M\ddot{x}+C\dot{x}+Kx=f_v(t)} \tag{15}$$

In the formula: is the system's vibration displacement vector; and represent the vibration velocity and acceleration vectors respectively; is the system's equivalent dynamic excitation vector, where the dynamic excitation mainly originates from: comprehensive meshing error excitation, time-varying meshing stiffness excitation, and external load excitation. Therefore, it can be expressed as

$$f_v(t)=f_e(t)+f_k(t)+f_L(t) \tag{16}$$

The excitation is caused by meshing error,$f_k(t)$ is time-varying meshing stiffness and is external load.

The equation (15) is the vibration dynamic equation of the system, which describes the vibration response characteristics of the system under dynamic excitation.

According to the theory of vibration dynamics, the vibration power flow is defined as the product of the applied force and the structural vibration velocity. The instantaneous vibration power flow of the system can be expressed as

$$P(t)=f_v^T(t)\dot{x}(t) \tag{17}$$

where: $P(t)$ is the instantaneous vibration power of the system; is the equivalent excitation vector; is the vibration velocity vector.

Substituting the vibration dynamics equations (17) into equation (13), we obtain the power balance relationship of the system's vibration:

$$P(t)=\ddot{x}^T M\dot{x}+\dot{x}^T C\dot{x}+x^T Kx \tag{18}$$

where $\dot{x}^T M\ddot{x}=\frac{d}{dt}\left(\frac{1}{2}\dot{x}^T M\dot{x}\right)$ denotes the rate of change of the system's kinetic energy, and denotes the rate of change of the system's elastic potential energy. Thus, the power balance equation for system vibration can be expressed as:

$$P(t)=\frac{d}{dt}\left(\frac{1}{2}\dot{x}^{T}M\dot{x}+\frac{1}{2}x^{T}Kx\right)+\dot{x}^{T}C\dot{x} \tag{19}$$

where: The first term represents the rate of change of the system's kinetic energy, the second term represents the rate of change of the system's potential energy, and the third term represents the damping dissipation power. This formula indicates that part of the input vibration power is converted into changes in the system's kinetic and potential energy, while the other part is dissipated through damping.

2.3 Parametric Method of profile modification

Cycloidal profile modification adjusts the gear tooth profile to improve the meshing state and reduce transmission error and meshing impact. Specifically, appropriate profile modifications at the tooth tip and root can help alleviate sharp contact during initial engagement and edge contact during final meshing, thereby improving load distribution uniformity and meshing smoothness. This treatment is beneficial to transmission stability and may help alleviate stress concentration associated with manufacturing tolerances and assembly deviations. Tooth profile modification is a precision modification of gear tooth tips and roots, which removes interference caused by meshing errors and effectively mitigates impact during gear engagement [17].

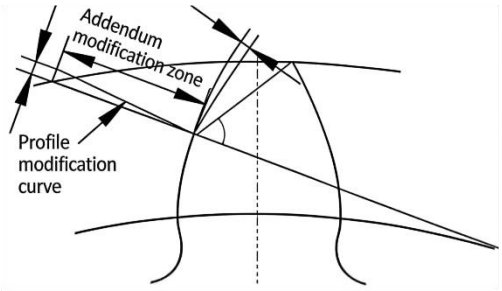

Figure 3. Tooth Profile Modification

Helical profile modification, also known as tooth direction modification, involves minor adjustments along the tooth direction from both ends of the tooth. This method reduces the impact of shaft bending deformation on the load distribution of the gear teeth, ensuring a more uniform load distribution along the tooth direction and thereby improving the gear's fatigue life. Common helical profile modification techniques include tooth direction drumming, tooth direction beveling, and parabolic profile modification. In engineering practice, drumming is typically employed to facilitate precise gear machining, as illustrated in Figure 4.

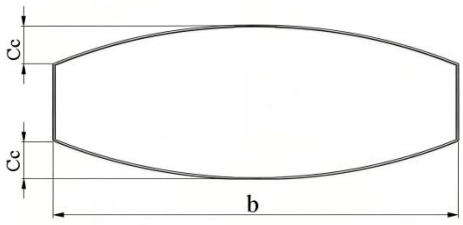

Figure 4. Drum-shaped Trimming

For drum-shaped modification, $\frac{b_{ca1}}{b}<1$, $b_{ca1}=\sqrt{\frac{2F_m b}{F_y C_\gamma}}$: At that time, the trimming amount is calculated as:

$$C_c=\sqrt{\frac{2F_m F_{\beta y}}{bC_\gamma}} \tag{20}$$

Accordingly $\frac{b_{ca1}}{b}>1$, the modification amount can be expressed as:

$$C_c=0.5F_{\beta y}+\frac{F_m}{bC_\gamma} \tag{21}$$

where: F_m is the circumferential force; is the tooth width; is the tooth stiffness; is the tooth meshing skew angle. Romax software provides an automated optimization toolkit for gear profile modification, enabling parameter analysis and automated iterative processes that outperform formula-based calculations in computational efficiency [17]. This study utilizes Romax's algorithmic solution for profile parameter errors. The second-generation Romax Genetic Algorithm (GGA) represents an enhanced iteration of the original GGA, incorporating more complex mutation codes. It overcomes the limitations of the original GGA by preventing trapped states during genetic mutation calculations, while generating all possible variable permutations after genetic recombination. The second-generation GGA incorporates crossover mutations, enabling frequent optimization of optimal configurations. This approach improves design quality through iterative refinement and introduces new designs in each generation.

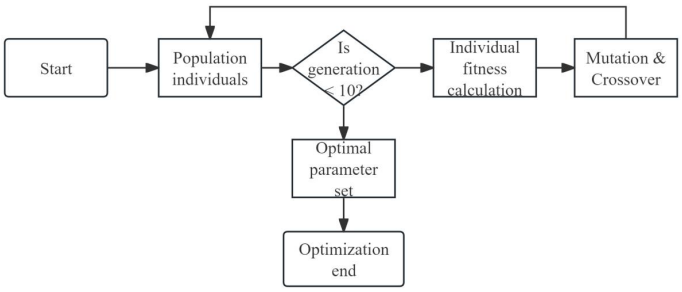

Figure 5. Flowchart of the Second-generation Genetic Algorithm Optimization Process

Define the genetic population. Select an appropriate population size while avoiding excessive population size that may lead to unnecessary complexity in crossover and mutation processes. Set the number of generations to

5, the population size to 20 per generation, the mutation coefficient to 0.3, and the crossover coefficient to 0.2. The defined population is shown in Figure 6.

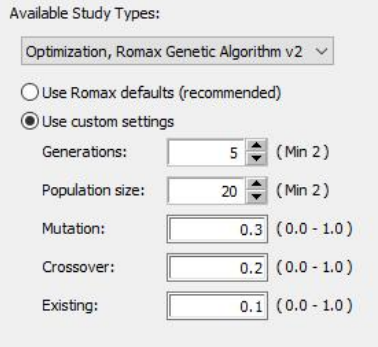

Figure 6. Optimization Parameters of the Second-generation Genetic Algorithm

The cycloid gear and pin gear in cycloid-pin gear transmission form conjugate meshing, and the tooth profile is formed by rolling the cylindrical surface in the center circle of pin gear. According to the transmission principle of cycloid-pin, the standard tooth profile equation of cycloid-pin is obtained as follows:

$$\begin{cases} x=R_z\left[sin\left(\frac{\theta_b}{z_a}\right)-\frac{K_1}{z_b}sin\left(\frac{z_b\theta_b}{z_a}\right)\right]+r_z cos\gamma \\ y=R_z\left[cos\left(\frac{\theta_b}{z_a}\right)-\frac{K_1}{z_b}cos\left(\frac{z_b\theta_b}{z_a}\right)\right]-r_z sin\gamma \end{cases} \tag{22}$$

Among:

$$\begin{cases} cos\gamma=\dfrac{K_1 sin(z_b\phi)-sin\phi}{\sqrt{1+K_1^2-2K_1 cos(z_a\phi)}} \\ sin\gamma=\dfrac{-K_1 cos(z_b\phi)+cos\phi}{\sqrt{1+K_1^2-2K_1 cos(z_a\phi)}} \end{cases} \tag{23}$$

Where: is the radius of the needle tooth center circle; is the radius of the pinion teeth; is the number of cycloidal wheel teeth; is the number of pinion teeth; is the short pitch coefficient; is the relative rotation angle of the rounding; is the rotation angle of the rounding center around the base circle center.

The combined moved-distance and equidistance modification method has been widely used in engineering practice.This method achieves tooth profile modification by simultaneously changing the center-circle radius and the tooth radius.

The trimmed parameters are:

$$\begin{cases} R_{z'}=R_z-\Delta R_z \\ r_{z'}=r_z-\Delta r_z \end{cases} \tag{24}$$

ΔR_z is the distance of the moved distance and is the distance of the equidistance modification.

The equation of the cycloid tooth profile after trimming is:

$$\begin{cases} x=R_{z'}\left[sin\left(\frac{\theta_b}{z_a}\right)-\frac{K_1}{z_b}sin\left(\frac{z_b\theta_b}{z_a}\right)\right]+r_{z'}cos\gamma \\ y=R_{z'}\left[cos\left(\frac{\theta_b}{z_a}\right)-\frac{K_1}{z_b}cos\left(\frac{z_b\theta_b}{z_a}\right)\right]-r_{z'}sin\gamma \end{cases} \tag{25}$$

where:

$$K_1=\frac{az_b}{R_{z'}}$$

where: is the eccentricity; is the number of pin teeth

The center circle of the needle tooth is changed by the shift distance modification, and the overall clearance of the tooth profile is changed by the equidistance modification.

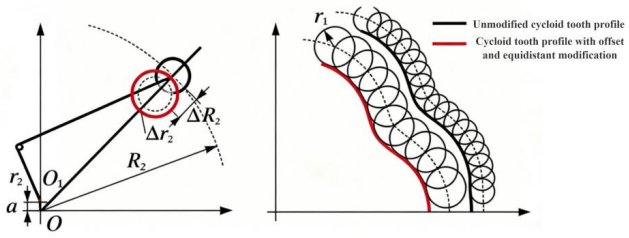

Figure 7. Principle Diagram of Isometric Modification with Variable Spacing

A pressure-angle-based cycloidal tooth profile modification method reported in our previous work is adopted here as one of the compared modification strategies [18]. As an important parameter related to meshing characteristics, the pressure angle during cycloidal-to-pinion meshing is defined as the angle between the force direction at the meshing point and the velocity direction at that point. Based on the standard cycloidal tooth profile equation, the derived expression for the pressure angle is:

$$\alpha_i=arccos\left(\frac{dy_i}{\sqrt{dx_i^2+dy_i^2}}\cdot\frac{-y_i}{\sqrt{x_i^2+y_i^2}}+\frac{-dx_i}{\sqrt{dx_i^2+dy_i^2}}\cdot\frac{x_i}{\sqrt{x_i^2+y_i^2}}\right) \tag{26}$$

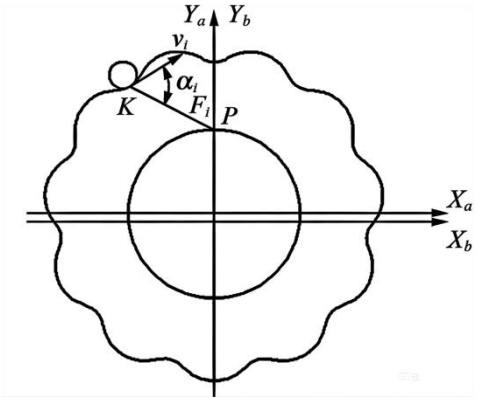

Figure 8. Schematic Diagram of Pressure Angle

The analysis of the pressure-angle variation indicates that the pressure angle is relatively large near the tooth root and tooth tip, which may be unfavorable for meshing performance. Therefore, profile modification is introduced in these regions to improve the meshing condition. In order to ensure that cycloidal gear maintains the standard conjugate transmission relationship in the working range and forms proper clearance in the tooth top and tooth root areas, a pressure-angle-based segmented profile modification method is adopted.

The cycloidal tooth profile is divided into three regions:

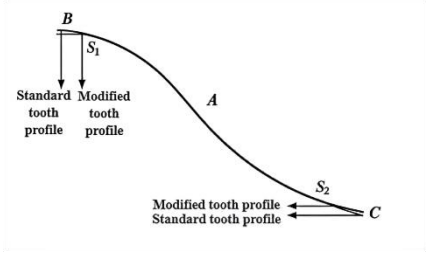

Figure 9. Arcuate Tooth Profile Zoning Diagram (A Working Zone; B Tooth Tip Modification Zone; C tooth Root Modification Zone)

The standard cycloidal tooth profile is still used in the working range:

$$\begin{cases} x=R_z\left[sin\left(\frac{\theta_b}{z_a}\right)-\frac{K_1}{z_b}sin\left(\frac{z_b\theta_b}{z_a}\right)\right]+r_z cos\gamma \\ y=R_z\left[cos\left(\frac{\theta_b}{z_a}\right)-\frac{K_1}{z_b}cos\left(\frac{z_b\theta_b}{z_a}\right)\right]-r_z sin\gamma \end{cases} \tag{27}$$

For non-working intervals, the tooth profile is modified by changing the pin-tooth radius radius. Therefore,

$$r_z=r_z+dr_z \tag{28}$$

The tooth profile equation after trimming is:

$$\begin{cases} x=R_z\left[sin\left(\frac{\theta_b}{z_a}\right)-\frac{K_1}{z_b}sin\left(\frac{z_b\theta_b}{z_a}\right)\right]+(r_z+dr_z)cos\gamma \\ y=R_z\left[cos\left(\frac{\theta_b}{z_a}\right)-\frac{K_1}{z_b}cos\left(\frac{z_b\theta_b}{z_a}\right)\right]-(r_z+dr_z)sin\gamma \end{cases} \tag{29}$$

Root modification function:

$$dr_z=D_0+D_1\theta_b+D_2\theta_b^2$$

Crown trimming function:

$$dr_z=G_0+G_1\theta_b+G_2\theta_b^2$$

The constant of are determined by the boundary conditions. This modification method maintains continuous and smooth tooth profiles at the junctions, which is beneficial to meshing stability.

2.4 Evaluation Index of Vibration Power Flow

To visualize the system's vibration changes more clearly, we convert both force and velocity into harmonic oscillation quantities. Under steady-state harmonic vibration conditions, the system response is defined as

$$x(t)=Re(Xe^{j\omega t}) \tag{30}$$

Where the displacement amplitude vector is and the excitation angular frequency is ω.

Then the frequency domain velocity is

$$V(\omega)=j\omega X \tag{31}$$

The vibration power flow, defined as the average instantaneous power over the shortest period of a periodic vibration, can be expressed in the frequency domain as

$$P(\omega)=\frac{1}{2}Re\left(V^{H}(\omega)\cdot\ F(\omega)\right) \tag{32}$$

where Re(*) denotes the real part of the complex number, denotes the frequency-domain force, denotes the frequency-domain velocity, and *H denotes the conjugate transpose.

The vibration power flow can be expressed in power level (dB(A)) form:

$$L_P=10lg\frac{P}{P_0} \tag{33}$$

where L_P Wis the vibration power level; is the vibration power flow;P_0 is the power reference,$P_0=1\times10^{-12}$.

In the formula (32), both force and velocity are complex numbers, so the vibration power flow considers the force, velocity and their phase relationship, which can evaluate the vibration performance more effectively. Meanwhile, as a scalar, the vibration power flow can consider the vibration in different directions of the system.To obtain the vibration-noise-related response under different operating conditions, the steady-state dynamic response of the system is first solved from Eq. (15) using the Gill integration method. The resulting vibration velocity response and equivalent excitation are then transformed into the frequency domain to obtain V(ω) and F(ω). Substituting these quantities into Eq. (32) yields the vibration power flow in the frequency domain, and Eq. (33) is further used to convert it into a power-level form. In the present study, this power-level quantity is used as an equivalent acoustic-radiation-power index for comparative evaluation of the vibration-noise-related behavior of the RV reducer. The results shown in Figure 10 and 11 are obtained in this manner.

2.5 Numerical Solution and Parameter Setting

In the numerical solution of differential equations for gear system dynamics, commonly used methods include the Newmark method, Runge–Kutta method, Gill method, and shooting method. The Runge–Kutta method, derived from the Taylor series expansion principle, is well suited for strongly nonlinear equations and, in its implicit form, can also handle stiff systems. However, it generally requires longer computation time and stricter convergence conditions, with the variable-step fourth-order Runge–Kutta method being the most widely used form. In comparison, the Newmark method is more suitable for response analysis of multi-degree-of-freedom gear systems, whereas the Runge–Kutta method is better suited to single gear-pair dynamic models with fewer degrees of freedom [14,19,20]. In this study, the Gill integration method is adopted as an improved form of the Runge–Kutta method, offering smaller truncation errors, faster integration, and lower computational cost [20].

The second-generation genetic algorithm of Romax optimized 100 candidate solutions, with the resulting tooth direction drum shape and inclination, as well as the optimal remodification parameters shown in Table 1. The remodification parameters provided by the corporate partner are listed in Table 2, while the dynamic analysis parameters are presented in Table 3.

Table 1. Profile Parameters of Involute Gear

Tooth Surface	Lead Crown Modification(μm)	Profile Crown Modification(μm)
Right	2	5
Left	3	5

Table 2. Cycloid–Pin Crowning Parameters

Pinion Center Radius(mm)	77	
Pinion Radius(mm)	3	
Eccentricity(mm)	1.5	
Cycloidal Tooth Number	39	
Pinion Tooth Number	40	
Displacement Crowning Parameters	moved distance modification Crowning Amount(mm)	0.027
	equidistance modification Crowning Amount(mm)	0.022
Pressure Angle Crowning Parameters	Addendum Crowning Pressure Angle(°)	65
	Addendum Crowning Amount(mm)	0.045
	Dedendum Crowning Pressure Angle(°)	75
	Dedendum Crowning Amount(mm)	0.015

Table 3. Dynamic Analysis Parameters

Parameter Setting	Value
Input Gear Shaft Speed(r/min)	1500
Average Gear Mesh Stiffness(N/m)	9.0×10^{8}
Amplitude of Time-Varying Gear Mesh Stiffness (N/m)	1.1×10^{7}
Assigned Gear Pair Contact Damping (Ns·/m)	500
Cycloid–Pin Contact Stiffness (N/m)	3.2×10^{8}
Cycloid–Pin Contact Damping (Ns·/m)	500

Parameter Setting	Value
Rolling Element Contact Stiffness of Carrier Bearing (N/m)	5.1×10^8
Radial Contact Stiffness of Supporting Bearing Rolling Elements (N/m)	1.6×10^8
Rolling Element–Raceway Contact Damping (Ns·/m)	500
Rated Load Torque(Nm·)	800
Gravitational Acceleration (m/s²)	9.8
Numerical Calculation Method	Gill Integration Method
Integration Time Step (ms)	0.01

3. Trend Comparison Under Different Operating Conditions

3.1 Model Parameters and Operating Conditions

Taking the RV80E reducer for as the analysis object, this reducer has a transmission ratio of 81. Its geometric structural parameters are shown in Table 4, while the mass inertia parameters of transmission components are listed in Table 5. For conventional gear transmission systems, as input speed changes, not only does the gear meshing state change, but the system's meshing frequency and its harmonic components also vary. Meanwhile, load torque does not alter the distribution of frequency components across excitation sources, only affecting their amplitudes in a linear manner. However, RV reducers exhibit characteristics such as simultaneous multi-tooth engagement, minimal meshing impact, and smooth transmission, which fall under typical low-frequency vibration conditions. Therefore, noise sensitivity to rotational speed is lower than that of conventional planetary gear reducers. Based on Ref. [21], the operating condition table shown in Table 6 are defined. According to references [14,22-24], operating conditions under different loads at rated speeds and different speeds under rated loads are considered. Additionally, according to Ref. [24], the vibration and noise of RV reducers may be more sensitive to load variations, leading to the design of Condition 7.

Table 4. Geometric Structural Parameters of the RV Reducer

Transmission Component	Geometric Design Parameter	Value
Involute Gear	Number of Input Gear Teeth	16

Transmission Component	Geometric Design Parameter	Value
	Number of Planet Gear Teeth	32
	Module (mm)	1.75
Cycloid–Pin Wheel	Eccentricity(mm)	1.5
	Pin Radius(mm)	3
	Radius of Pin Teeth Distribution Circle(mm)	77
	Number of Pin Teeth	40
	Number of Cycloid Gear Teeth	39
Carrier Bearing	Inner Diameter (mm)	30
	Outer Diameter(mm)	36
	Roller Diameter (mm)	5
	Number of Rollers	14
Supporting Bearing	Inner Diameter (mm)	15
	Outer Diameter (mm)	35
	Roller Diameter(mm)	5
	Number of Rollers	14

Table 5 Mass and Inertia Parameters of Transmission Components

Transmission Component	Mass m(kg)	Moment of Inertia J ($kg{\cdot}mm^{2}{\cdot}$)
Input Gear Shaft	0.12	7.24
Planet Gear and Crankshaft Assembly	0.13	13.81

Transmission Component	Mass m(*kg*)	Moment of Inertia J ($kg{\cdot}mm^{2}{\cdot}$)
Cycloidal Disc	0.22	378
Output Disc and Clamping Plate Assembly	1.6	2288

Table 6. Operating Conditions

Index	Output Speed(*rpm*)	Carrier Load($Nm{\cdot}$)
1	15	800
2	5	800
3	30	800
4	40	800
5	15	2000
6	15	400
7	200	800

3.2 Trend Comparison Under Different Operating Conditions

The results presented in Figure 10 and 11 are theoretical predictions obtained from Eqs. (32) and (33). Specifically, the steady-state vibration response under each operating condition is first solved from the coupled dynamic equation, and the corresponding vibration power level is then calculated in the frequency domain according to Eq. (32) and converted into dB(A) form using Eq. (33). Therefore, these two figures represent the vibration-noise-related response predicted by the present theoretical model, rather than direct outputs from Romax.

As shown in Figure 10(a), under the rated load of 800 N·m, the calculated vibration power level changes only slightly when the output speed varies from 5 rpm to 40 rpm, indicating weak sensitivity of the vibration-noise-related response to speed variation within the low-speed operating range. Figure 10(b) is a local enlargement of Figure 10(a), which more clearly highlights the small differences among the low-speed conditions. A more noticeable increase appears when the output speed rises to 200 rpm, suggesting that the response level becomes higher outside the main low-speed operating range.

Figure 11 shows the corresponding results under different load conditions at an output speed of 15 rpm. Compared with the relatively small speed-induced variation, the vibration power level increases much more evidently with load, indicating that load has a stronger influence on the vibration-noise-related response of the

RV reducer under the investigated conditions. This trend is physically consistent with the multi-tooth meshing and high-load transmission characteristics of the RV reducer. Therefore, within the present operating range, the system response is characterized by weak sensitivity to low-speed variation but relatively high sensitivity to load increase.

These results provide the theoretical operating-condition background for the subsequent comparative analysis of profile-modification schemes.

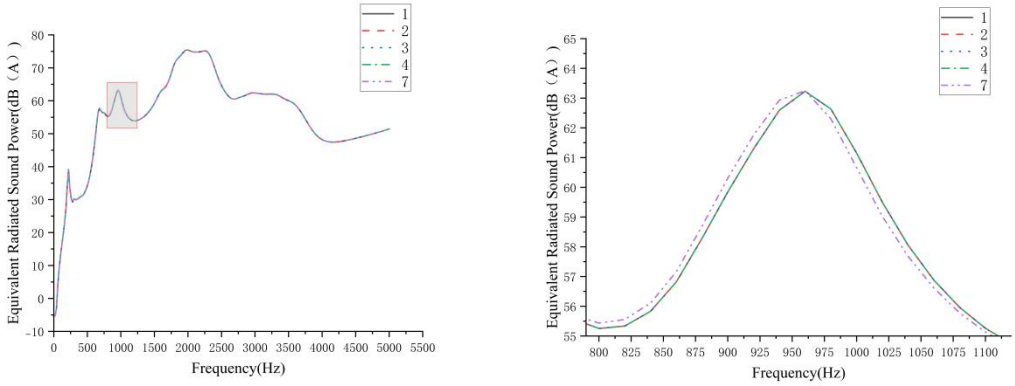

(a) **full operating range** **(b) enlarged view of the low-speed range (5–40 rpm).**

Figure 10. Calculated Vibration Power Level under Different Output Speeds at a Carrier Load of 800 N·m

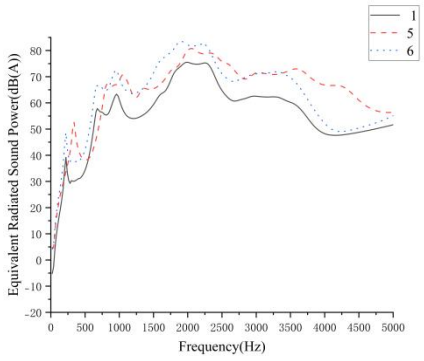

Figure 11. Calculated Vibration Power Level under Different Carrier Loads at an Output Speed of 15 rpm

As shown in Figure 10, under the rated load of 800 N·m, the equivalent acoustic radiation power varies only slightly as the output speed increases from 5 to 40 rpm, indicating weak sensitivity to speed within the low-speed operating range, whereas a more noticeable increase appears at 200 rpm. In contrast, Figure 11 shows that, at 15 rpm, the equivalent acoustic radiation power increases more significantly with load, suggesting that load has a stronger effect on the vibration-noise-related response of the RV reducer under the investigated conditions. Therefore, within the present operating range, the system exhibits limited sensitivity to low-speed variation but relatively strong sensitivity to load increase. These results provide the

operating-condition background for the subsequent profile-modification analysis.

4. Discussion of Profile Modification Effects

The operating-condition trends shown in Figures 10 and 11 are obtained directly from the theoretical dynamic model through Eqs. (32) and (33), which establishes the vibration-response framework and operating-condition dependence of the RV reducer. On this basis, the influence of profile modification is further investigated within the same coupled dynamic framework with the support of Romax-based contact analysis. In the present study, Romax is employed to obtain contact-related parameters under different modification schemes, including meshing stiffness variation, load distribution, contact stress, and transmission-related contact characteristics. These results are used to support the interpretation of how profile modification alters excitation characteristics and load-transfer behavior, rather than being treated as an independent alternative to the theoretical model.

Accordingly, the following discussion is organized into three parts: first, the effect of involute profile modification on the meshing stiffness variation of the primary stage; second, the influence of two cycloidal modification strategies on the contact stress and transmission behavior of the secondary stage; and finally, the whole-machine response in terms of transmission error and equivalent acoustic radiation power.

4.1 Influence of Involute Profile on Primary Meshing Stiffness and Load Distribution

As the first step of the Romax-based comparative analysis, the influence of involute profile modification on the primary meshing characteristics is analyzed. Figure 12 compares the total meshing stiffness of the involute gear pair before and after profile modification. In the unmodified case, the stiffness reaches a maximum of approximately N/mm and then drops sharply to about N/mm during the transition from double-tooth to single-tooth engagement, corresponding to a local reduction of about 47.4%. Such an abrupt change indicates strong stiffness fluctuation and implies an increased tendency for impact excitation during the meshing transition.

After involute profile modification, the maximum meshing stiffness decreases to approximately N/mm, which is about 17.3% lower than that of the unmodified case. More importantly, the stiffness curve becomes noticeably smoother, and the abrupt change in the single-to-double tooth transition region is significantly weakened. The sudden stiffness rise near the meshing-out stage is also suppressed. These results indicate that the main benefit of involute modification is not a higher absolute stiffness level, but a reduction in stiffness fluctuation and transition discontinuity. From a dynamic point of view, this is beneficial to smoother load transfer, weaker parametric excitation, and improved meshing stability of the primary stage.

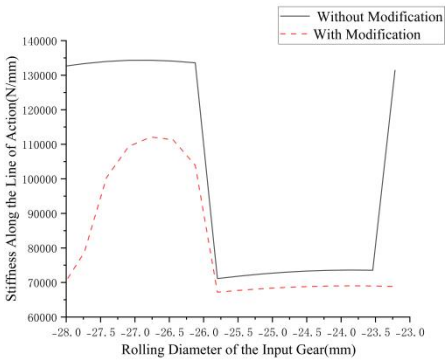

Figure 12. Comparison of Total Engagement Stiffness of End Faces Before and After Profile Modification of Involute Gear

4.2 Influence of Two Types of Cycloid Modification on Secondary Contact Stress and Bearing State

As shown in Figure 13, the cycloidal profile modification strategy has a pronounced influence on the contact stress distribution of the cycloid-pin stage. For the theoretical profile without cycloidal modification, the peak contact stress is approximately 1000 MPa. After applying the moved-distance equidistant modification, the peak stress increases to about 1600 MPa, corresponding to an increase of roughly 60% relative to the unmodified profile. This result indicates that the load becomes more concentrated on fewer contact teeth, which is unfavorable for the load-carrying capacity and fatigue performance of the transmission.

By contrast, the pressure-angle modification limits the peak contact stress to about 1100 MPa. Compared with the moved-distance equidistant scheme, this represents a reduction of approximately 31.3%, while the increase relative to the theoretical profile is only about 10%. Although both modification schemes alter the contact pattern, the pressure-angle modification produces a much less severe stress concentration and a more uniform load transfer in the meshing region. Therefore, under the present conditions, pressure-angle modification exhibits a more favorable contact state than the moved-distance equidistant scheme, particularly in terms of limiting peak stress and improving load distribution uniformity.

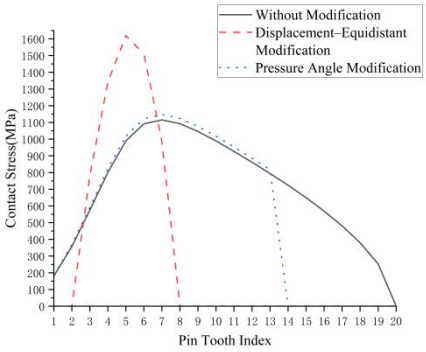

Figure 13. Comparison of contact stress before and after cycloidal gear remodification

4.3 Influence of Different Forming Combinations on the Transmission Error of the Whole Machine

Figure 14 compares the whole-machine transmission error under different profile-modification combinations. In the baseline case without cycloidal modification, the transmission error is approximately 30.2″. When involute profile modification is combined with the cycloidal moved-distance equidistant modification, the transmission error increases to about 31.5″, i.e., an increase of 1.3″ or about 4.3% relative to the baseline case. This indicates that, although the modification scheme changes the contact condition, it does not improve the overall transmission accuracy under the present operating condition.

When the cycloidal pressure-angle modification is used instead, the transmission error decreases to approximately 30.9″. This value is 0.6″ lower than that of the moved-distance equidistant scheme, corresponding to a reduction of about 1.9%, although it is still 0.7″ higher than the baseline case, i.e., about 2.3% above the unmodified level. Therefore, the absolute difference among the three cases is limited, but the pressure-angle modification recovers part of the transmission-error increase caused by the alternative cycloidal modification. Combined with the lower contact stress concentration observed in Figure 13, this result suggests that pressure-angle modification is more effective in maintaining transmission stability and meshing continuity at the whole-machine level.

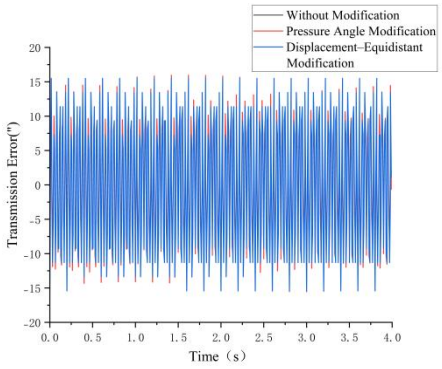

Figure 14. Comparison of Transmission Error for the Entire Machine

4.4 Effect of Different Modification Combinations on Equivalent Acoustic Radiation Power

Figure 15 presents the equivalent acoustic radiation power level of the entire machine for three profile-modification configurations. In the baseline configuration, a pronounced low-frequency maximum of approximately 71 dB(A) is observed at around 800 Hz, accompanied by several subsidiary peaks in the medium- and high-frequency bands. With the involute and displaced-equidistant modification, the dominant low-frequency peak is reduced to about 69 dB(A), corresponding to a decrease of approximately 2 dB(A) relative to the baseline. Nevertheless, its overall benefit remains limited, as the band-averaged acoustic radiation power level over 1500-3000 Hz increases slightly from roughly 72 dB(A) to 73 dB(A), suggesting that the reduction achieved by this scheme is confined to a relatively narrow portion of the spectrum.

By comparison, the involute and pressure-angle modification exhibits a substantially stronger broad dB(A) suppression effect. Specifically, the dominant low-frequency peak decreases to approximately 60 dB(A), which

is about 11 dB(A) lower than that of the baseline configuration and 9 dB(A) lower than that of the involute and displaced-equidistant case. Meanwhile, the band-averaged equivalent acoustic radiation power level in the medium- and high-frequency ranges decreases by about 4 dB(A) and 3 dB(A), respectively. Over the full investigated frequency range, the integrated equivalent acoustic radiation power is reduced by approximately 60% relative to the baseline configuration. These results demonstrate that the involute and pressure-angle modification provides the most effective mitigation of the system's vibroacoustic response among the three configurations considered.

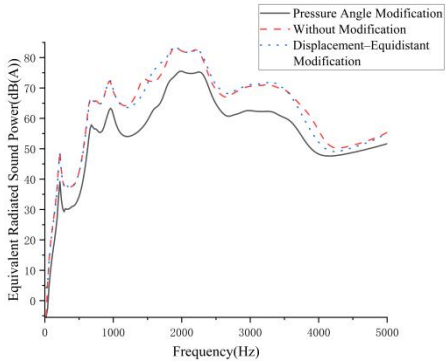

Figure 15. Comparison of acoustic radiation power indices for different modification combinations

4.5 Discussion of Mechanism

Vibration and noise in RV reducers originate from the coupled effects of composite meshing errors, time-varying meshing stiffness, and external loads in the multistage transmission system. Tooth profile modification affects vibro-acoustic performance by altering tooth contact geometry and load transfer paths, thereby influencing both excitation intensity and vibration energy transmission. For involute gear pairs, profile and lead modifications can smooth the stiffness variation during the transition between single- and double-tooth engagement, improve load distribution along the line of action, and reduce meshing impact as well as stiffness-related excitation. For cycloid-pin gear pairs, equidistance modification under load may decrease the number of load-sharing pins, resulting in load concentration and increased contact stress. By contrast, pressure-angle modification improves meshing transition through local adjustment of the tooth tip and root while maintaining conjugate action in the working region, which promotes smoother load transfer and alleviates stress concentration. From a system-level coupling perspective, involute profile modification mainly suppresses first-stage stiffness fluctuation, whereas pressure-angle optimization improves second-stage load distribution. Their coordinated application reduces the transfer of dynamic excitation to the support structure and lowers vibration power input to the system. As a result, the equivalent acoustic radiation power decreases while transmission error remains relatively stable. These findings indicate that coordinated profile optimization, viewed from the perspective of energy transfer, is an effective approach for the low-noise design of RV reducers.

5. Conclusion

This study established a coupled multi-body dynamic model of an RV reducer by integrating the involute gear pair, cycloid-pin pair, and bearing-support system, and comparatively evaluated the effects of different profile modification schemes using contact-related parameters extracted from Romax. The results show that involute profile modification primarily influences the first meshing stage by smoothing the variation of meshing stiffness. Under the investigated condition, the maximum meshing stiffness decreases from approximately N/mm to1.10×10^5 N/mm after modification, corresponding to a reduction of about 17.3%, while the abrupt stiffness transition between single-tooth and double-tooth engagement is significantly alleviated, indicating improved meshing smoothness and reduced impact tendency.

For the cycloid-pin stage, the two modification strategies exhibit markedly different contact characteristics. Compared with the theoretical profile, the moved-distance equidistant modification causes evident load concentration and increases the peak contact stress to about 1600 MPa. By contrast, pressure-angle modification limits the peak contact stress to approximately 1100 MPa, which is about 31.3% lower than that of the moved-distance equidistant scheme, while also maintaining a more uniform stress distribution.

At the whole-machine level, the transmission error is about 30.2″ in the baseline case, increases to 31.5″ under the involute plus moved-distance equidistant modification scheme, and decreases to 30.9″ under the involute plus pressure-angle modification scheme. Although the absolute reduction in transmission error is limited, the pressure-angle-based combination exhibits more stable fluctuation characteristics and lower equivalent acoustic radiation power over the investigated frequency range, suggesting superior overall dynamic performance. These findings indicate that the effect of profile modification in an RV reducer should be interpreted from the perspective of system coupling: involute modification mainly suppresses first-stage stiffness fluctuation, whereas cycloidal pressure-angle modification improves second-stage load transfer and stress distribution. Their coordinated application is therefore beneficial for reducing dynamic excitation transmission and improving the vibration-noise performance of the entire reducer.

This study is mainly based on theoretical modeling and numerical simulation. Experimental validation of transmission error, vibration, and noise responses under representative operating conditions will be carried out in future work to further verify the proposed analysis framework.

References

[1] Pham A, Ahn H. High Precision Reducers for Industrial Robots Driving 4th Industrial Revolution: State of Arts, Analysis, Design, Performance Evaluation and Perspective [J]. International Journal of Precision Engineering and Manufacturing-Green Technology, 2018, 5(4): 519-533.

[2] Duc P A, Joon A H. Rigid Precision Reducers for Machining Industrial Robots [J]. International Journal of Precision Engineering and Manufacturing, 2021, 22(8): 1469-1486.

[3] Wang S, et al. Study on Torsional Vibration of RV Reducer Based on Time-Varying Stiffness [J]. Journal of Vibration Engineering & Technologies, 2020, 9(1): 1-12.

[4] Xin X L, Kui C B, Yang L C. Dynamic modelling and contact analysis of

bearing-cycloid-pinwheel transmission mechanisms used in joint rotate vector reducers [J]. Mechanism and Machine Theory, 2019, 137: 432-458.

[5] Wang H, et al. Transmission Performance Analysis of RV Reducers Influenced by Profile Modification and Load [J]. Applied Sciences, 2019, 9(19).

[6] Li W, Zhang Y, Gao S. Analysis for time varying torsional stiffness of RV reducer [J]. Mechanical Systems and Signal Processing, 2025, 225: 112239.

[7] Yuhu Y, et al. A modelling approach for kinematic equivalent mechanism and rotational transmission error of RV reducer [J]. Mechanism and Machine Theory, 2021, 163.

[8] Lixin X, Chen X, Le C. Dynamic modeling and vibration analysis of an RV reducer with defective needle roller bearings [J]. Engineering Failure Analysis, 2024, 157: 107884.

[9] Liu Wenchuan, Zhang Yinghui, He Weidong. Research on Gear Profile Modification for Noise Reduction in RV Reducers Based on Orthogonal Experiments [J]. Mechanical Transmission, 2023, 47(5): 26-31.

[10] Huiliang W, et al. Transmission characteristics of an RV reducer based on ADAMS [J]. Journal of Mechanical Science and Technology, 2024, 38(2): 787-800.

[11] Gao S, et al. Piecewise Modification of Cycloidal Gear in RV Reducer: Application of Spline Interpolation Theory and Comparison with a Combination Modification Optimization Method [J]. International Journal of Precision Engineering and Manufacturing, 2024, 26(1): 1-14.

[12] Ronghua Z, Jianxing Z, Zheng W. Study on transmission error and torsional stiffness of RV reducer under wear [J]. Journal of Mechanical Science and Technology, 2022, 36(8): 4067-4081.

[13] Qiao Xuetao, et al. Effects of Two-stage Tooth Profile Modification on Vibration in RV Reducers [J]. Manufacturing Technology and Machine Tools, 2024(12): 62-71.

[14] Chang Lehao. General Modeling Method for Dynamics of Parallel-axle Gear Transmission Systems and Research on Dynamic Excitation Effects [D]. Northwestern Polytechnical University, 2014.

[15] Xu Lixin, Yang Yuhu. A method for analyzing the multi-tooth meshing contact characteristics of cycloid-pin transmission [J]. China Mechanical Engineering, 2016, 27(10): 1382-1388.

[16] Ye Xiaofen, et al. Analysis of Force in RV Transmission Mechanism [J]. Mechanical Transmission, 2019, 43(08): 107-115.

[17] Xu Yinlong. Simulation Analysis of the Traction Man-Gear Transmission System for EMUs Based on Romax [D]. Dalian Jiaotong University, 2023.

[18] Yue Lang, He Weidong, Zhang Yinghui. Pressure angle-based cycloidal tooth profile modification method [J]. Mechanical Transmission, 2020, 44(1): 35-40, 121.

[19] Liu L, et al. Dynamic modeling of fully coupled gearboxes and analysis of housing effects [J]. Journal of Harbin Engineering University, 2018, 39(03): 561-568.

[20] Yang Zhen. Research on Dynamic Characteristics of Torque-Shunt Gear Transmission Systems [D]. Xi'an: Northwestern Polytechnical University, 2007.

[21] Zhang Jieting, et al. Analysis of torsional vibration of RV reducer based on variational mode

decomposition [J]. Mechanical Strength, 2025, 47(03): 75-81.

[22] Liu Wenchuan. Dynamic Response and Noise Reduction of Precision Cycloidal Reducers for Robots [D]. Dalian Jiaotong University, 2023.

[23] Xu Jianmin, et al. Analysis of vibration characteristics of RV reducers considering rotational speed and load [J]. Journal of Jimei University (Natural Science Edition), 2023, 28(03): 259-266.

[24] Xu Lixin, Xia Chen, Yang Bo. Dynamic transmission error analysis and experiment of RV reducer under load conditions [J]. China Mechanical Engineering, 2023, 34(18): 2143-2152.

[25] Kaneko K, Kaminaga H, Sakaguchi T, et al. Humanoid Robot HRP-5P: An Electrically Actuated Humanoid Robot with High-Power and Wide-Range Joints [J]. IEEE Robotics and Automation Letters, 2019, 4(2): 1431-1438.